

## BLUNTNESSEFFECTS ON LIFT-TO-DRAG RATIO OF POWER-LAW BODIES IN RAREFIED HYPERSONIC AIRFLOW

Wilson F. N. Santos, wilson@lcp.inpe.br

National Institute for Space Research, Combustion and Propulsion Laboratory, Cachoeira Paulista-SP, 12630-000 BRAZIL

**Abstract.** *This paper deals with a numerical study of the aerodynamic surface quantities on power-law shaped leading edges situated in a rarefied hypersonic flow. The sensitivity of the heat flux to, and pressure gradient on the body surface due to changes on the angle of attack is investigated by using the Direct Simulation Monte Carlo (DSMC) method. A method that has demonstrated to yield excellent comparisons with experimental data, and that properly accounts for non-equilibrium aspects of the flow that arise near the nose of the leading edges and that are especially important at high Mach number. The work is motivated by interest in assessing the overall performance of power-law shaped leading edges in order to consider them as possible candidates for blunting geometries of hypersonic configurations. The results presented highlight the sensitivity of the heat flux, total drag, total lift and the lift-to-drag ratio to changes on the angle of attack. Comparison based on these properties are made between power-law shapes and a sharp-edged wedge.*

**Keywords:** *Hypersonic Flow, Rarefied Flow, DSMC, Power-Law Leading Edge.*

### 1. INTRODUCTION

The successful design of high-lift, low-drag hypersonic configurations will depend on the ability to incorporate relatively sharp leading edges that combine good aerodynamic properties with acceptable heating rates. The use of blunt-nose shapes tends to alleviate the aerodynamic heating problem since the heat transfer for blunt bodies is far lower than that for sharply pointed bodies. In addition, the reduction in heating rate for a blunt body is accompanied by an increase in heat capacity, due to the increased volume. Due mainly to manufacturing problems and the extremely high temperatures attained in hypersonic flight, hypersonic vehicles should have blunt nose, although probably slendering out at a short distance from the nose.

Certain hypersonic configurations, such as waveriders (Nonweiler, 1959), are designed analytically with infinitely sharp leading edges for shock wave attachment. Because the shock wave is attached to the leading edge of the vehicle, the upper and lower surfaces of the vehicle can be designed separately. Furthermore, this attached shock prevents spillage of higher pressure air from the lower side of the vehicle to the upper side. As a result of this attached shock, waveriders have been shown to have the potential to provide high values for the lift-to-drag ( $L/D$ ) ratio at high Mach numbers.

It is well known that very sharp leading edge is not practical for a number of reasons: (1) it is difficult to manufacture, (2) some blunting is required for structural strength, and (3) the heat transfer to the nose of the leading edge is severe at high Mach numbers. In this context, any practical waveriders should have some degree of bluntness dictated by either manufacturing or heating requirements. Therefore, designing a hypersonic vehicle leading edge involves a tradeoff between making the leading edge sharp enough to obtain acceptable aerodynamic and propulsion efficiency and blunt enough to reduce the aerodynamic heating at the stagnation point.

Power-law shaped leading edges ( $y \propto x^n, 0 < n < 1$ ) may provide the required bluntness for heat transfer and manufacturing concerns. This concept is based on the work of Mason and Lee (1994), who have pointed out that, for certain exponents, power-law shapes exhibit aerodynamic properties similar to geometrically sharp shapes. They suggested the possibility of a difference between shapes that are geometrically sharp and shapes that behave aerodynamically as if they were sharp. Mason and Lee (1994) showed that for values of  $0 < n < 1/2$ , the leading-edge radius of curvature goes to infinite at the nose, a characteristic of a blunt shape. For values of  $1/2 < n < 1$  the leading-edge radius of curvature approaches zero at the nose, a characteristic of a sharp shape. Furthermore, for  $2/3 < n < 1$ , their computational investigation predicts that the derivative of the pressure coefficient with respect to the body coordinate  $dC_p/ds$  approaches  $-\infty$  at  $x = 0$ , a characteristic of a sharp body. In this manner, there is a class of body shapes given by  $1/2 < n < 2/3$ , for which the leading edge may behave aerodynamically like a blunt body, even though the leading-edge radius of curvature is zero, and another one given by  $2/3 < n < 1$  for which the leading edge may behave like aerodynamically sharp body even though the leading edge bluntness is infinite. Their analysis describes the details of the geometry and aerodynamics of low-drag axisymmetric bodies by using Newtonian theory. However, one of the important aspects of the problem, stagnation point heat transfer, was not considered.

Based on recent interest in hypersonic waveriders for high-altitude/low-density applications, a great deal of experimental and theoretical works has been carried out previously on power-law form representing blunt geometries. Of particular interest are the works by O'Brien and Lewis (1999), Santos and Lewis (2002 and 2005) and by Santos (2008). The major interest in these works has gone into considering the power-law body as possible candidate for blunting geometries of hypersonic leading edges.

The sensitivity of the pressure gradient and the stagnation point heating to shape variations of power-law leading edges

was investigated by Santos and Lewis (2002) for the idealized situation of two-dimensional rarefied hypersonic flow at zero-degree angle of incidence. Through the use of DSMC method, they showed that the pressure gradient on the power-law shapes in a rarefied environment is in surprising agreement with that obtained by Mason and Lee (1994), obtained by employing Newtonian analysis. Santos and Lewis (2002) also found that the stagnation point heating behavior for power-law leading edges with finite radius of curvature ( $n = 1/2$ ), followed that predicted for classical blunt body in the continuum flow regime, i.e., the heating rate on blunt bodies scales inversely with the square root of the curvature radius at the stagnation point. For those power-law leading edges with zero radii of curvature ( $n > 1/2$ ), the stagnation point heating is not a function of the curvature radius in the vicinity of the leading edges, but surprising agrees with the classical blunt body behavior predicted by the continuum flow far from the stagnation point.

Santos and Lewis (2005) compared power-law shapes to round leading edges in order to determine which geometry would be better suited as a blunting profile by considering rarefied hypersonic flow. It was found that circular cylinder shapes provide smaller drag coefficient for equivalent stagnation point heating under the range of conditions investigated.

In the present account, the primary purpose is to investigate the impact of the angle of attack on the aerodynamic surface quantities. For positive angle of attack, important changes occur in the flowfield structure and in the aerodynamic surface quantities on blunt leading edges. This involves the modification of the flowfield properties and shock strength and, consequently, some effects on aerodynamic forces acting on, and on heat transfer to the body surface. Moreover, the knowledge of these properties at zero-degree angle of attack is not sufficient to predict with certainty the flow characteristics over these shapes with incidence. In this context, the essential characteristics of the angle-of-attack effect on heat flux, wall pressure, shear stress, total drag, total lift and the  $L/D$  ratio will be examined for power-law bodies defined by exponents of  $1/2$ ,  $2/3$ ,  $3/4$  and  $4/5$ , and positive angle of attack with  $0$ ,  $5$ ,  $10$ ,  $15$  and  $20$  degrees of incidence. In the current study, DSMC method will be employed to calculate the rarefied hypersonic two-dimensional flow.

## 2. LEADING-EDGE GEOMETRY DEFINITION

In dimensional form, the body power-law shapes are given by the following expression,

$$y = ax^n \quad (1)$$

where  $n$  is the power-law exponent and  $a$  is the power-law constant which is a function of  $n$ .

The power-law shapes are modeled by assuming a sharp-edged wedge of half angle  $\theta$  with a circular cylinder of radius  $R$  inscribed tangent to this wedge. The power-law shapes, inscribed between the wedge and the cylinder, are also tangent to them at the same common point where they have the same slope angle. The circular cylinder diameter provides a reference for the amount of blunting desired on the leading edges. It was assumed a leading-edge half angle of  $10$  degrees, a circular cylinder diameter of  $10^{-2}$ m and power-law exponents of  $1/2$ ,  $2/3$ ,  $3/4$  and  $4/5$ . Figure 1(a) illustrates schematically this construction for the set of power-law leading edges investigated.

From geometric considerations, the power-law constant  $a$  is obtained by matching slope on the wedge, circular cylinder and power-law body at the tangency point. The common body height  $H$  at the tangency point is equal to  $2R \cos \theta$ , and the body length  $L$  from the nose to the tangency point in the axis of symmetry is given by  $nH/2 \tan \theta$ . It was assumed that the power-law leading edges are infinitely long but only the length  $L$  is considered in the simulation since the wake region behind the power-law bodies is not of interest in this investigation.

## 3. COMPUTATIONAL METHOD AND PROCEDURE

A number of significant problems in fluid mechanics involve flows in the transitional regime, i.e., flows for which the Knudsen number  $Kn$  is larger than  $0.1$  and less than  $10$ . Knudsen number is the ratio of the molecular mean free path  $\lambda$  to a characteristic length  $l$ . The most accurate and credible numerical technique for modeling complex flows in the transitional regime has been the DSMC method conceived by Bird (1994). DSMC has been recognized as an extremely powerful technique capable of predicting an almost unlimited variety of rarefied flowfields in the regimes where neither the Navier-Stokes nor the free molecular approaches are appropriate.

The DSMC method simulates real gas flow with various physical processes by means of a huge number of modeling particles, each of which is a typical representative of great number of real gas molecules. DSMC models the flow as being a collection of discrete particles, each one with a position, velocity and internal energy. The state of the particles is stored and modified with time as the particles move, collide, and undergo boundary interactions in simulated physical space, which is represented by a computational cell network.

A fundamental assumption in the DSMC method is that the gas is dilute, i.e., the mean molecular diameter is much less than the mean molecular spacing of molecules in the gas. This feature of the DSMC method allows that the molecular motion and collisions are uncoupled over the period of a specific time step. In this way, the predictions of the new positions of the molecules as well as the resulting boundary interactions are followed by the selection of a set of possible intermolecular collisions that are appropriate during the time step. In general, the simulation time, discretized into time steps, is identified with the physical time of the real flow, and the time step should be sufficiently small in comparison

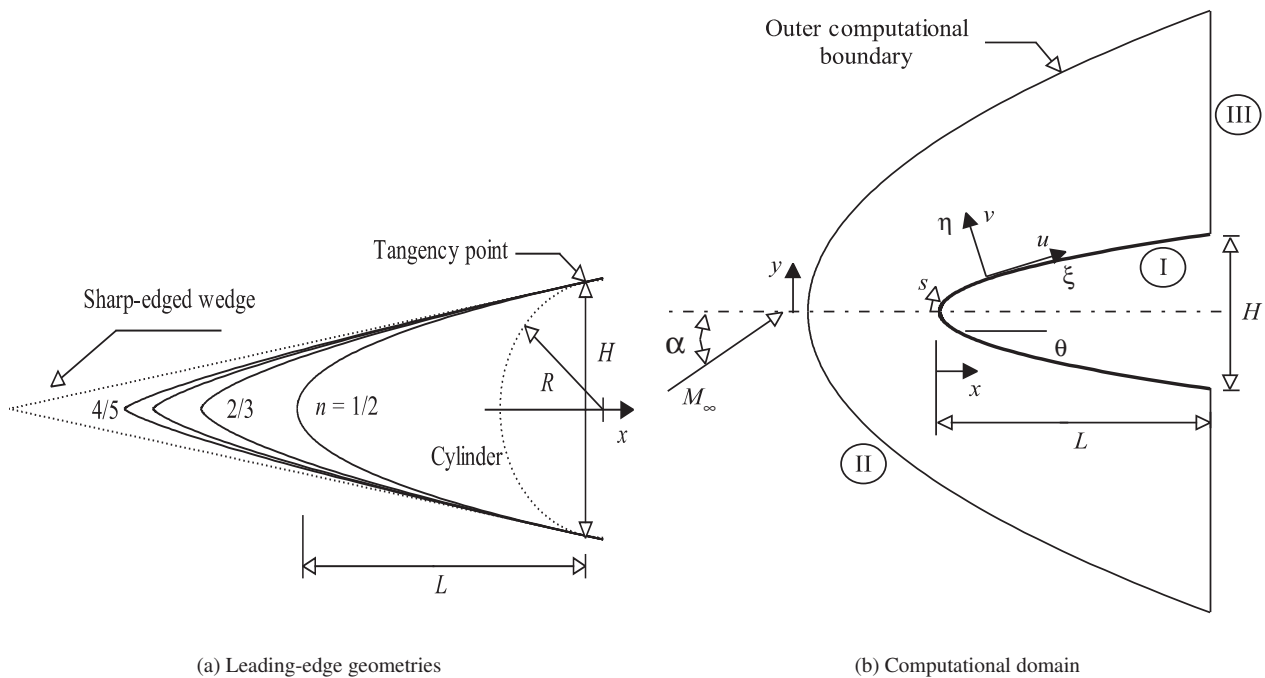


Figure 1. Drawing illustrating (a) the leading edge geometries and (b) The computational domain.

with the local mean collision time.

The molecular collisions are simulated with the variable hard sphere (VHS) molecular model (Bird, 1981) and the no time counter (NTC) collision sampling technique (Bird, 1989). The VHS model employs the simple hard sphere angular scattering law so that all directions are equally possible for post-collision velocity in the center-of-mass frame of reference. However, the collision cross section depends on the relative speed of colliding molecules. The energy exchange between kinetic and internal modes is controlled by the Borgnakke-Larsen statistical model (Borgnakke and Larsen, 1975). The essential characteristic of this model is that a fraction of the collisions is treated as completely inelastic, and the remainder of the molecular collisions is regarded as elastic. Simulations are performed using a non-reacting gas model consisting of two chemical species,  $N_2$  and  $O_2$ . Energy exchanges between the translational, rotational and vibrational modes are considered. For this study, constant relaxation numbers of 5 and 50 were used for the rotation and vibration, respectively, and the effective number of degrees of freedom in the partially excited vibrational states was calculated from the harmonic oscillator theory.

The flowfield is divided into a number of regions, which are subdivided into computational cells. The cells are further subdivided into 4 subcells, 2 subcells/cell in each direction. The cell provides a convenient reference sampling of the macroscopic gas properties, while the collision partners are selected from the same subcell for the establishment of the collision rate. As a result, the flow resolution is much higher than the cell resolution. The dimensions of the cells must be such that the change in flow properties across each cell is small. The linear dimensions of the cells should be small in comparison with the scale length of the macroscopic flow gradients normal to the streamwise directions, which means that the cell dimensions should be of the order of the local mean free path or even smaller.

The computational domain used for the calculation is made large enough so that body disturbances do not reach the upstream and side boundaries, where freestream conditions are specified. A schematic view of the computational domain is depicted in Fig. 1(b). Side I is defined by the body surface. Diffuse reflection with complete thermal accommodation is the condition applied to this side. In this model, the reflection of the impinging molecules is not related to the pre-impingement state of the molecules. The outgoing velocity of the molecules is randomly assigned according to a half-range Maxwellian distribution determined by the wall temperature. Side II is the freestream side through which simulated molecules enter and exit. Finally, the flow at the downstream outflow boundary, side III, is predominantly supersonic and vacuum condition is specified (Bird, 1994). At this boundary, simulated molecules can only exit.

Numerical accuracy in DSMC method depends on the grid resolution chosen as well as the number of particles per computational cell. Both effects were investigated to determine the number of cells and the number of particles required to achieve grid independence solutions for the thermal non-equilibrium flow that arises near the nose of the leading edges. Grid independence was tested by running the calculations with half and double the number of cells in  $\xi$  and  $\eta$  directions (see Fig. 1(b)) compared to a standard grid. Solutions (not shown) were near identical for all grids used and

Table 1. Freestream flow conditions

Altitude (km)	$T_\infty$ (K)	$p_\infty$ (N/m <sup>2</sup> )	$\rho_\infty$ (kg/m <sup>3</sup> )	$\mu_\infty$ (Ns/m <sup>2</sup> )	$n_\infty$ (m <sup>-3</sup> )	$\lambda_\infty$ (m)
70	220.0	5.582	$8.753 \times 10^{-5}$	$1.455 \times 10^{-5}$	$1.8209 \times 10^{21}$	$9.03 \times 10^{-4}$

were considered fully grid independent.

The freestream and flow conditions employed in the present calculations are those given by Santos and Lewis (2002) and listed in Tab. 1, and the gas properties (Bird, 1994) considered in the simulation are shown in Tab. 2. The freestream velocity  $V_\infty$  is assumed to be constant at 3.56 km/s, which corresponds to freestream Mach number  $M_\infty$  of 12. The wall temperature  $T_w$  is assumed constant at 880 K. The freestream Knudsen number corresponds to  $Kn_\infty = 0.0903$ , where the characteristic dimension was defined as being the diameter of the circular cylinder. Finally, the freestream Reynolds number by unit meter  $Re_\infty$  is 21455.

Table 2. Gas properties

	$X$	$m$ (kg)	$d$ (m)	$\omega$
$O_2$	0.237	$5.312 \times 10^{-26}$	$4.01 \times 10^{-10}$	0.77
$N_2$	0.763	$4.650 \times 10^{-26}$	$4.11 \times 10^{-10}$	0.74

#### 4. COMPUTATIONAL RESULTS AND DISCUSSION

In order to assess the overall performance of power-law leading edges, this section will focus on the calculations of the aerodynamic surface quantities obtained from the DSMC results. Aerodynamic surface quantities of particular interest in the present account are number flux, heat transfer, pressure, skin friction, drag and lift. Therefore, the purpose of this section is to discuss and to compare differences in the profiles of these properties, expressed in coefficient form, due to variations not only on the angle of attack but also on the shape of the leading edges. As mentioned earlier, the simulations were performed for power-law exponents of 1/2, 2/3, 3/4 and 4/5 at 0, 5, 10, 15, and 20 degrees of incidence.

##### 4.1 Number Flux

The number flux  $N$  is calculated by sampling the molecules impinging on the surface by unit time and unit area. A flux is regarded as positive if it is directed toward the body surface. The dependence of the number flux on the angle of attack  $\alpha$  is shown in Figs. 2 and 3 for power-law exponents of 1/2 and 3/4, respectively. In this set of plots, distribution of the number flux is displayed separated along the leeward side and along the windward side of the leading edges. Also,  $N_f$  is the number flux  $N$  normalized by  $n_\infty V_\infty$ ,  $S$  is the arc length  $s$ , normalized by the freestream mean free path  $\lambda_\infty$ , measured from the symmetry axis of the leading edges, or stagnation point for the case of zero-degree angle of incidence. For comparison purpose, the number flux for power-law shapes by considering zero-degree angle of attack is also presented in this set of plots.

Referring to Figs. 2 and 3, it is observed that, as would be expected, for positive angle of attack, the number flux in general decreases on leeward side, due to the flow expansion, and increases on windward side of the leading edge, due to the flow compression. For the zero-degree angle of incidence, the number flux is maximum at the stagnation point. At incidence, the stagnation point moves from the symmetry axis to another station downstream along the windward side. For the  $n = 1/2$  case, the number flux presents a constant value along the both surfaces at the vicinity of the symmetry axis. As the power-law exponent increases, i.e., as the leading edge becomes sharp, this behavior is not observed anymore.

##### 4.2 Heat Transfer Coefficient

The heat transfer coefficient  $C_h$  is defined as follows,

$$C_h = \frac{q_w}{\rho_\infty V_\infty^3 / 2} \quad (2)$$

where the heat flux  $q_w$  to the body surface is calculated by the net energy flux of the molecules impinging on the surface. The net heat flux  $q_w$  is related to the sum of the translational, rotational and vibrational energies of both incident and reflected molecules as defined by,

$$q_w = q_i + q_r = \sum_{j=1}^N \left[ \frac{1}{2} m_j c_j^2 + e_{Rj} + e_{Vj} \right]_i + \sum_{j=1}^N \left[ \frac{1}{2} m_j c_j^2 + e_{Rj} + e_{Vj} \right]_r \quad (3)$$

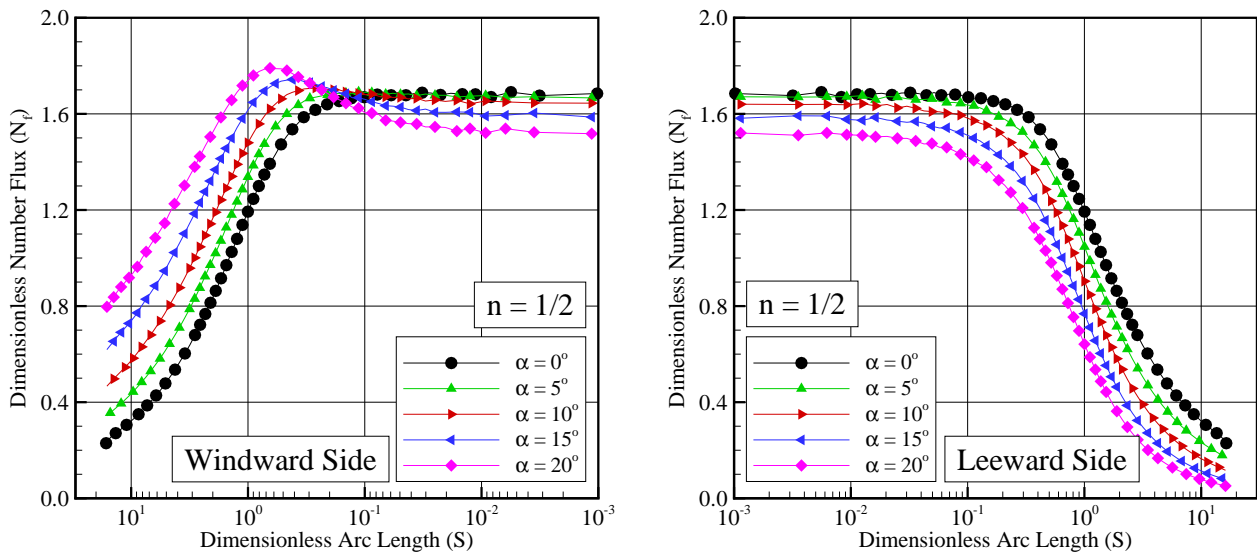


Figure 2. Dimensionless number flux  $N_f$  along the (a) windward side and (b) leeward side as a function of the angle of attack  $\alpha$  for power-law exponent  $n$  of 1/2.

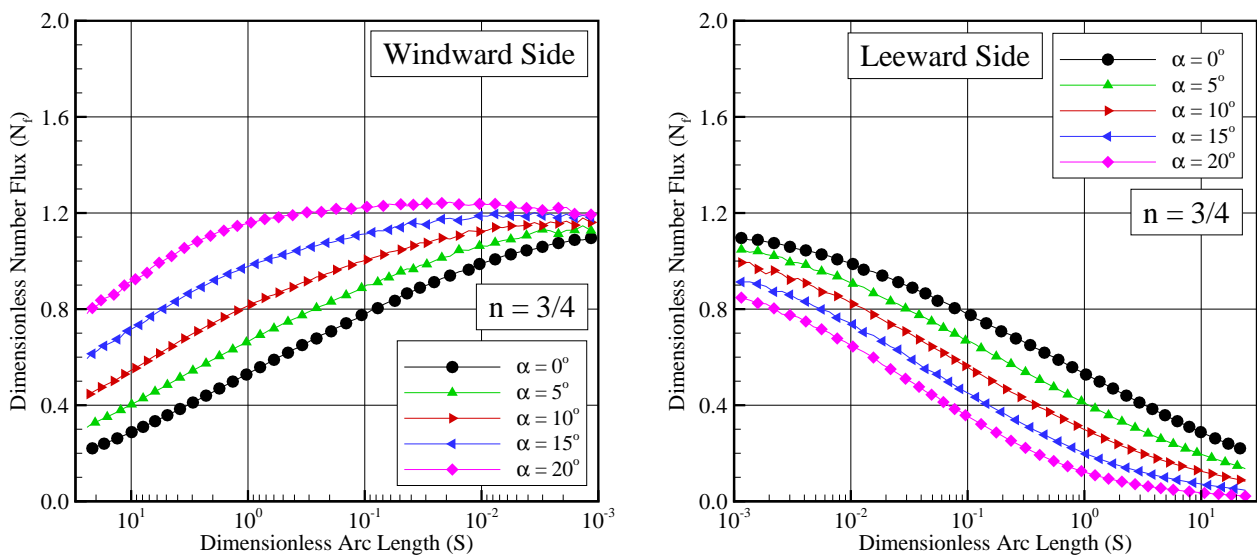


Figure 3. Dimensionless number flux  $N_f$  along the (a) windward side and (b) leeward side as a function of the angle of attack  $\alpha$  for power-law exponent  $n$  of 3/4.

where  $N$  is the number of molecules colliding with the surface by unit time and unit area,  $m$  is the mass of the molecules,  $c$  is the velocity of the molecules,  $e_R$  and  $e_V$  stand for the rotational and vibrational energies, respectively. Subscripts  $i$  and  $r$  refer to incident and reflect molecules.

The heat flux  $q_w$  to the body surface was defined in terms of the incident and reflected flow properties, and based upon the gas-surface interaction model of fully accommodated, complete diffuse re-emission. The diffuse model assumes that the molecules are reflected equally in all directions, quite independently of their incident speed and direction. Due to the diffuse reflection model, the reflected thermal velocity of the molecules impinging on the surface is obtained from a Maxwellian distribution that takes into account for the temperature of the body surface. In this fashion, as the wall temperature is the same for all the cases investigated, the number of molecules impinging on the surface plays the important role on the reflected contribution to the net heat flux to the body surface.

The leading-edge shape effect on heat transfer coefficient  $C_h$  is illustrated in Figs. 4 and 5 for power-law exponent  $n$  of 1/2 and 3/4, respectively, parameterized by the angle of attack  $\alpha$ . It is seen from these figures that the heat transfer coefficient  $C_h$  is sensitive not only to the power-law shape but also to the angle of attack. Similar to the number flux distribution, two distinct regions are observed in these plots. One inner region close to the stagnation point, where the heat transfer coefficient is approximately constant. However, the magnitude of the heat transfer coefficient on this region

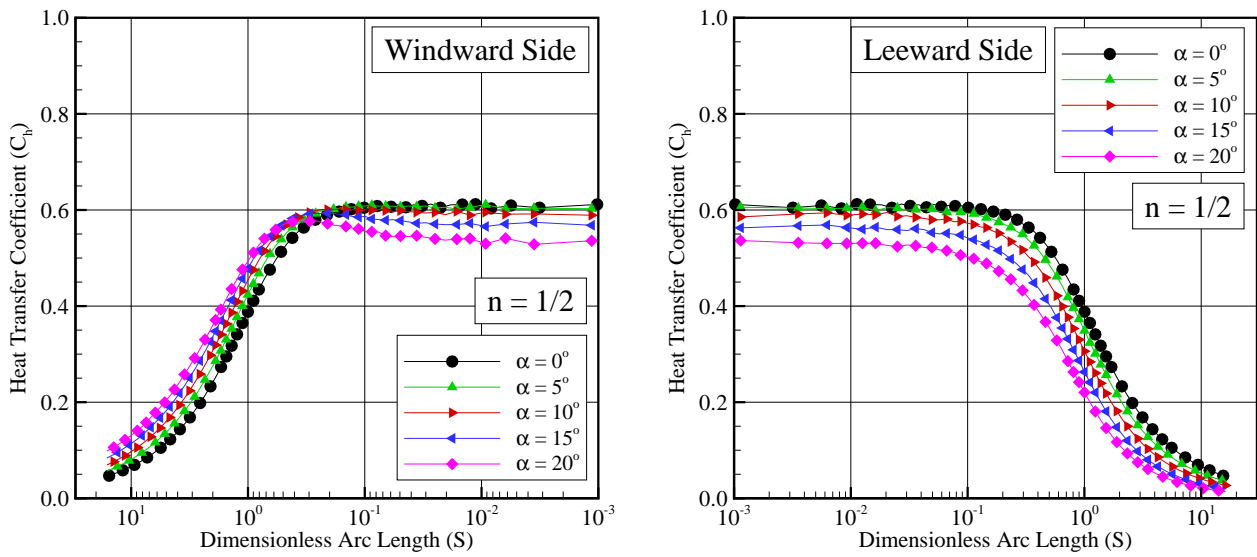


Figure 4. Heat transfer coefficient  $C_h$  along the (a) windward side and (b) leeward side as a function of the angle of attack  $\alpha$  for power-law exponent  $n$  of 1/2.

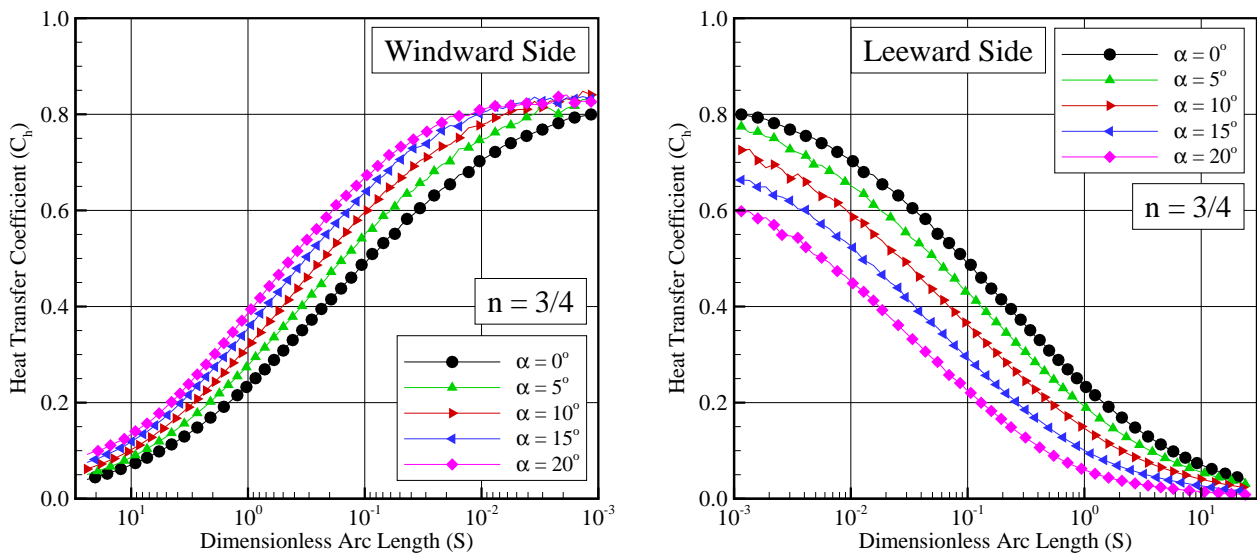


Figure 5. Heat transfer coefficient  $C_h$  along the (a) windward side and (b) leeward side as a function of the angle of attack  $\alpha$  for power-law exponent  $n$  of 3/4.

decreases with increasing the power-law exponent. Moreover, the extent of this region diminishes as the leading-edge shape becomes sharp. In the outer region, the heat transfer coefficient drops off downstream along the body surface. The angle-of-attack effect on the heat transfer coefficient along the body surface is similar to that for the number flux in the sense that it decreases on the leeward side and increases on the windward side of the leading edges.

### 4.3 Pressure coefficient

The pressure coefficient  $C_p$  is defined as being,

$$C_p = \frac{p_w - p_\infty}{\rho_\infty V_\infty^2 / 2} \quad (4)$$

where the pressure  $p_w$  on the body surface is calculated by the sum of the normal momentum fluxes of both incident and reflected molecules at each time step as follows,

$$p_w = p_i + p_r = \sum_{j=1}^N \{ [m_j c_{\eta j}]_i + [m_j c_{\eta j}]_r \} \quad (5)$$

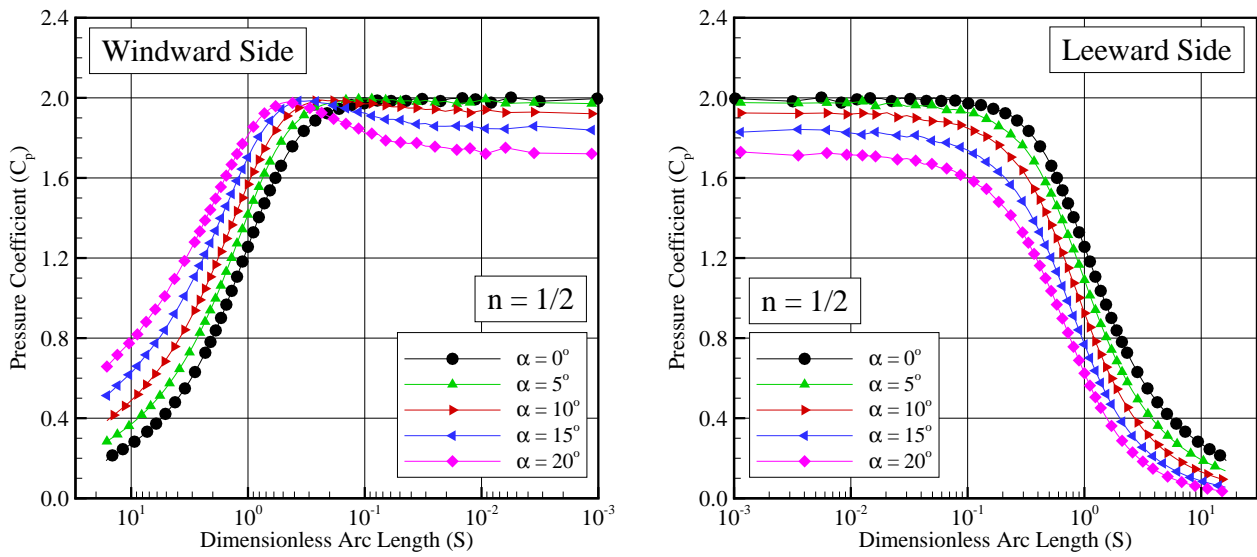


Figure 6. Pressure coefficient  $C_p$  along the (a) windward side and (b) leeward side as a function of the angle of attack  $\alpha$  for power-law exponent  $n$  of  $1/2$ .

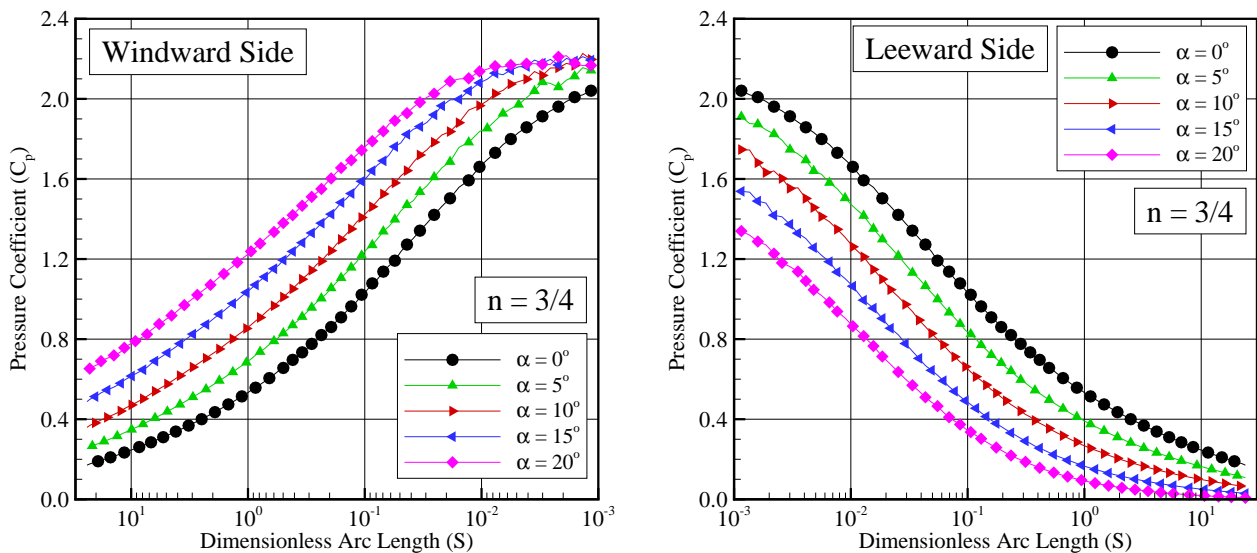


Figure 7. Pressure coefficient  $C_p$  along the (a) windward side and (b) leeward side as a function of the angle of attack  $\alpha$  for power-law exponent  $n$  of  $3/4$ .

where  $c_\eta$  is the normal velocity component of the molecules.

The dependence of the pressure coefficient due to variations in the angle of attack is demonstrated in Figs. 6 and 7 for power-law exponents of  $1/2$  and  $3/4$ , respectively.

According to these figures, by increasing the incidence causes the expected asymmetry in the pressure coefficient as the stagnation point moves from the axis to the lower windward side. The pressure coefficient presents the expected behavior in that it increases in the windward side and decreases in the leeward side with increasing the angle of attack  $\alpha$ .

#### 4.4 Skin Friction Coefficient

The skin friction coefficient  $C_f$  is defined as follows,

$$C_f = \frac{\tau_w}{\rho_\infty V_\infty^2 / 2} \quad (6)$$

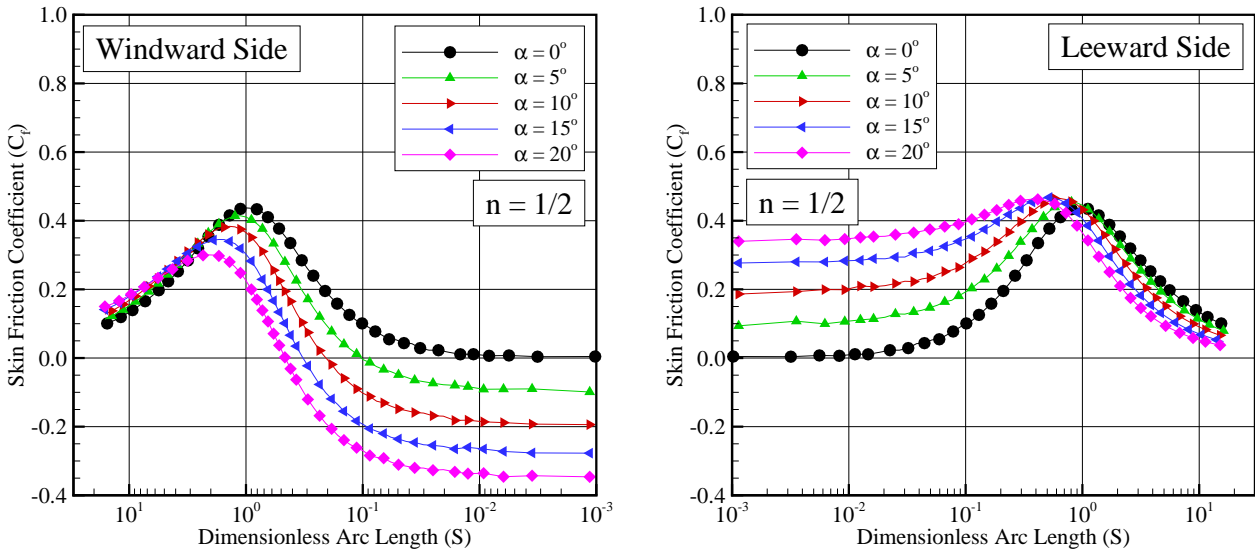


Figure 8. Skin Friction coefficient  $C_f$  along the (a) windward side and (b) leeward side as a function of the angle of attack  $\alpha$  for power-law exponent  $n$  of 1/2.

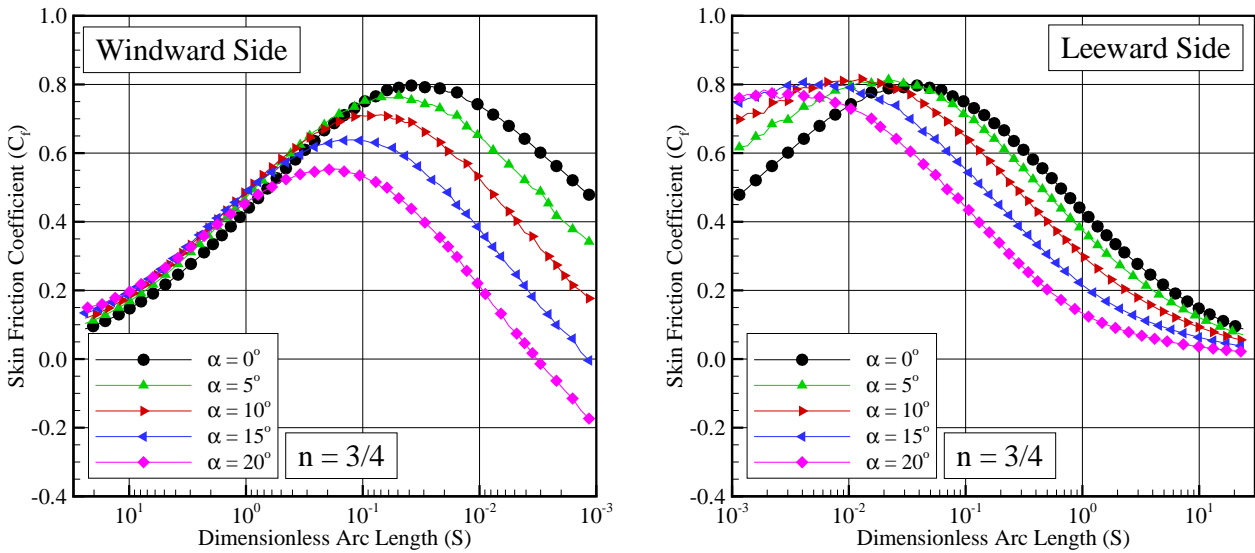


Figure 9. Skin Friction coefficient  $C_f$  along the (a) windward side and (b) leeward side as a function of the angle of attack  $\alpha$  for power-law exponent  $n$  of 3/4.

where the shear stress  $\tau_w$  on the body surface is calculated by the sum of the tangential momentum fluxes of both incident and reflected molecules impinging on the surface at each time step by the following expression,

$$\tau_w = \tau_i + \tau_r = \sum_{j=1}^N \{ [m_j c_{\xi j}]_i + [m_j c_{\xi j}]_r \} \quad (7)$$

where  $c_\xi$  is the tangential velocity component of the molecules.

It is worthwhile to note that, for the special case of diffuse reflection, the reflected molecules have a tangential moment equal to zero, since the molecules essentially lose, on average, their tangential velocity components. In this context, the contribution of the reflected tangential momentum flux  $\tau_r$ , which appears in Eq.(7), is equal to zero. Nevertheless, for incomplete surface accommodation, the reflected tangential momentum flux  $\tau_r$  contributes to the skin friction coefficient.

The dependence of the skin friction coefficient attributed to variations on the leading-edge shape and on the angle of attack is displayed in Figs. 8 and 9 for power-law exponents  $n$  of 1/2 and 3/4, respectively. According to these figures, the skin friction coefficient increases from a minimum value at the symmetry axis up to a maximum value at a station that corresponds to approximately a slope angle of 45 degrees. It is also noted that, at incidence, the distribution for the skin friction coefficient  $C_f$  is preserved, as compared to the case of zero-degree angle of incidence, in that it presents a

Table 3. Total drag coefficient  $C_d$ , (lift coefficient  $C_l$ ), and [lift-to-drag ratio  $L/D$ ] for the leading edges as a function of the angle of attack  $\alpha$ .

$\alpha$	$n = 1/2$	$n = 2/3$	$n = 3/4$	$n = 4/5$
$0^\circ$	1.176 (0.000) [0.000]	1.078 (0.000) [0.000]	1.044 (0.000) [0.000]	1.027 (0.000) [0.000]
$5^\circ$	1.197 (0.178) [0.148]	1.103 (0.256) [0.232]	1.072 (0.287) [0.268]	1.057 (0.304) [0.287]
$10^\circ$	1.254 (0.352) [0.281]	1.179 (0.510) [0.433]	1.155 (0.573) [0.496]	1.143 (0.608) [0.532]
$15^\circ$	1.349 (0.519) [0.384]	1.307 (0.757) [0.579]	1.296 (0.854) [0.659]	1.289 (0.909) [0.705]
$20^\circ$	1.481 (0.673) [0.454]	1.490 (0.990) [0.664]	1.502 (1.121) [0.746]	1.507 (1.194) [0.793]

minimum value at the symmetry axis, increases to a maximum value and then decreases downstream along the both body surfaces.

#### 4.5 Total Drag Coefficient

The total drag coefficient is defined as being,

$$C_d = \frac{F_D}{\rho_\infty V_\infty^2 H/2} \quad (8)$$

where  $F_D$  is the resultant force acting on the body surface, and  $H$  is the height at the matching point common to the leading edges (see Fig. 1).

The drag on a surface in a gas flow results from the interchange of momentum between the surface and the molecules colliding with the surface. In this fashion, the resultant force  $F_D$  acting on the body surface was obtained by the integration of the pressure  $p_w$  and shear stress  $\tau_w$  distributions in the flow direction from the symmetry axis of the leading edges to the station  $L$  that corresponds to the tangential point common to all shapes. It is worthwhile to mention that the values for the total drag coefficient were obtained by assuming the shapes acting as leading edges. As a result, no base pressure effects were taken into account on the calculations. Results for total drag are presented as total drag coefficient  $C_d$  and its components of pressure drag coefficient  $C_{pd}$  and the skin friction drag coefficient  $C_{fd}$ .

The impact of the leading-edge bluntness and the angle of attack on the total drag coefficient  $C_d$  is demonstrated in Figs. 10(a-b) for power-law exponent  $n$  of 1/2 and 3/4, respectively. In this group of diagrams, the pressure drag  $C_{pd}$ , skin friction drag  $C_{fd}$  and total drag  $C_d$  for power-law shaped leading edges are compared to the sharp-edged wedge case (Fig. 1). Therefore, full symbols stand for the sharp leading edge and empty symbols for power-law leading edges. For completeness, the results for total drag coefficient are tabulated in Tab. 3.

Interesting features may be seen in Fig. 10 as well as in Tab. 3. By considering the cases with zero-degree angle of incidence, it is clearly noticed that the major contribution to the total drag  $C_d$  is given by the skin friction drag  $C_{fd}$ . As the leading edge becomes blunter, the contribution of the pressure drag  $C_{pd}$  to the total drag increases and the contribution of the skin friction drag  $C_{fd}$  decreases. As a result of these to opposite behaviors, a small change is observed in the total drag coefficient for the power-law shapes investigated. It is seen that the total drag decreases as the power-law exponent increases from 1/2 to 4/5. It means that the leading edge is changing from blunt to sharp leading edge. On the other hand, as would be expected, appreciable changes are observed in the total drag coefficient  $C_d$  with the angle-of-attack rise. By increasing the angle of attack, the leading edges are seen from the freestream as blunt bodies. Consequently, the contribution of the pressure drag  $C_{pd}$  to the total drag  $C_d$  increases significantly while the skin friction drag contribution slightly decreases. A balance on these two contributions is observed for the  $n = 3/4$  case with approximately 14-degree angle of incidence. In contrast, for a 20-degree angle of incidence, the total drag coefficient  $C_d$  increases as the power-law exponent  $n$  increases from 1/2 to 4/5. A opposite behavior is presented for the same leading edges for zero-degree angle of incidence, as confirmed by Tab. 3.

#### 4.6 Total Lift Coefficient

The total lift coefficient is defined as being,

$$C_l = \frac{F_L}{\rho_\infty V_\infty^2 H/2} \quad (9)$$

where  $F_L$  is the resultant force acting on the body surface, and  $H$  is the height at the matching point common to the leading edges (see Fig. 1).

The lift force is obtained by the integration of the pressure  $p_w$  and shear stress  $\tau_w$  distributions from the stagnation

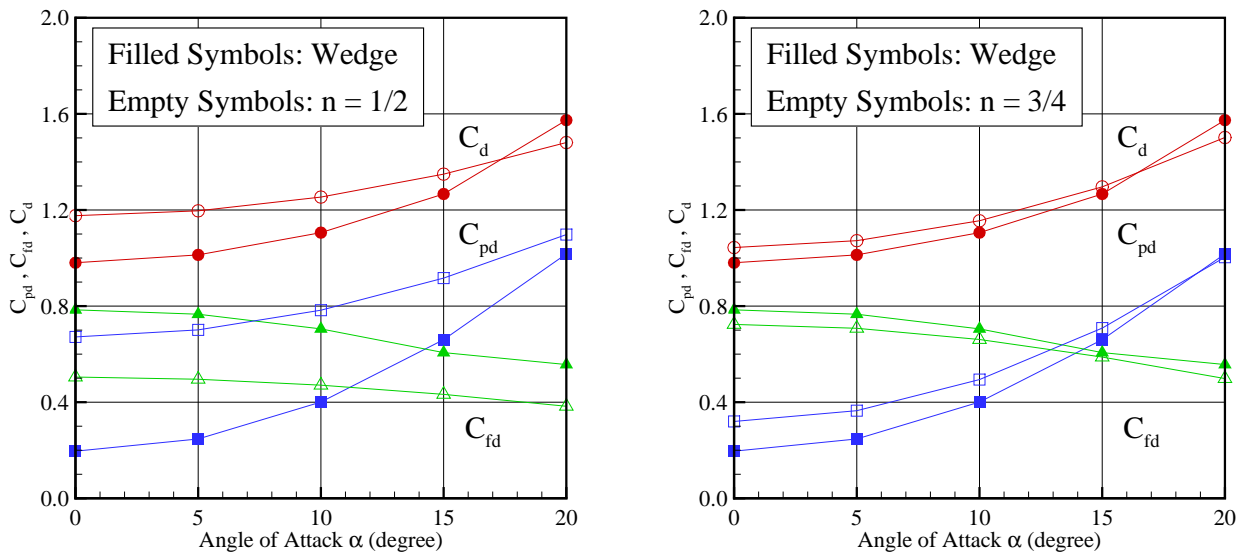


Figure 10. Pressure drag  $C_{pd}$ , skin friction drag  $C_{fd}$  and total drag  $C_d$  coefficients as a function of the angle of attack for power-law exponent  $n$  of (a) 1/2 and (b) 3/4.

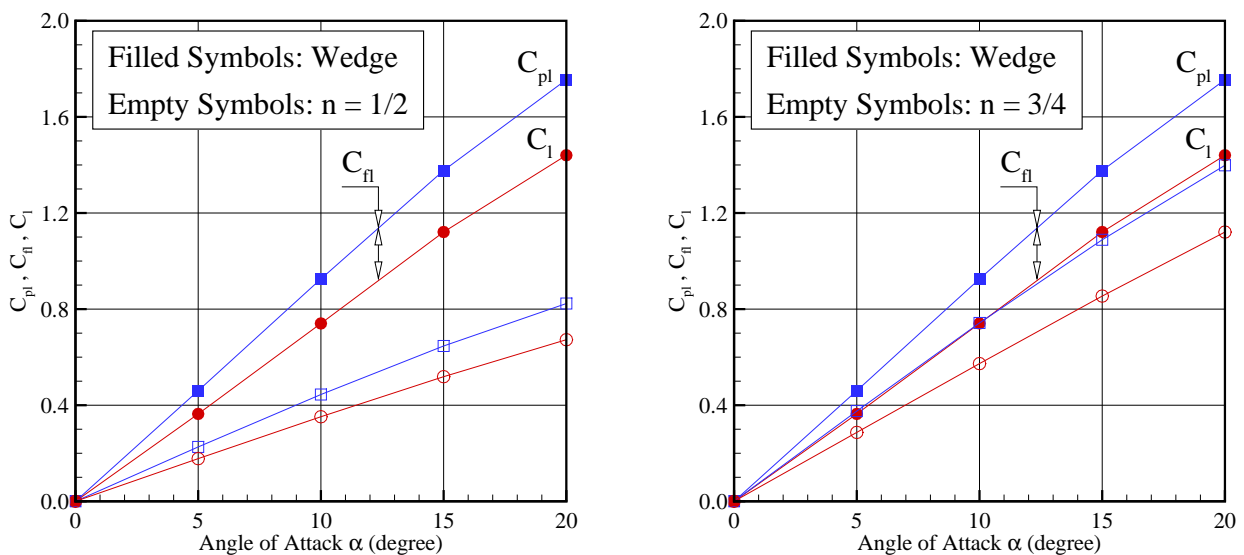


Figure 11. Pressure lift  $C_{pl}$ , skin friction lift  $C_{fl}$  and total lift  $C_l$  coefficients as a function of the angle of attack for power-law exponent  $n$  of (a) 1/2 and (b) 3/4.

point of the leading edge to the station  $L$  in the normal direction of the flow. Results for total lift coefficient are presented as total lift coefficient  $C_l$  and its components of pressure lift coefficient  $C_{pl}$  and the skin friction lift coefficient  $C_{fl}$ .

The extent of changes on total lift coefficient  $C_l$  due to variation on the leading-edge shape and on the angle of attack is illustrated in Figs. 11(a-b) for power-law exponent  $n$  of 1/2 and 4/5, respectively. In a similar way, in this set of diagrams, full symbols stand for the sharp-edged wedge and empty symbols for power-law leading edges. For convenience, Table 3 tabulates the total lift coefficient  $C_l$ , inside parenthesis, for all of the leading edges investigated.

Referring to Figs. 11(a-b) and Tab. 3, it is very encouraging to observe that appreciable changes results in the total lift coefficient  $C_l$  with changes on the leading-edge shape as well as on the angle of attack. As the power-law exponent  $n$  increases from 1/2 to 4/5, the total lift  $C_l$  increases, since the leading-edge shape changes from a blunt shape to a sharp one. This is explained by the fact that, as the leading edge becomes blunt, the shock-wave standoff increases. As a result, pressure air from the lower side of the leading edge communicates with the upper side between the shock wave and the nose of the leading edge, resulting in a reduction in the total lift.

In what follows, it becomes instructive to consider the lift-to-drag ( $L/D$ ) ratio. The  $L/D$  ratio as a function of the angle of attack is also tabulated in Tab. 3 by assuming zero base pressure, as mentioned earlier. For the sharp-edged wedge, the  $L/D$  ratio is 0.359, 0.669, 0.885 and 0.915 for angle of attack of 5, 10, 15 and 20 degrees, respectively.

Consequently, based on these values and on those in Tab. 3, for 5-degree angle of incidence, the  $L/D$  ratio for leading-edge shape corresponding to  $n$  of 1/2 and 4/5 is reduced approximately by 50% and 20%, respectively, as compared to that sharp-edged wedge. For 20-degree angle of incidence, the reduction on the  $L/D$  ratio for  $n$  of 1/2 and 4/5 is around 50% and 14%, respectively, as compared to that for sharp-edged wedge, at the same angle of incidence.

It is firmly established from the results for lift coefficient that the effect of either “aerodynamically” sharp leading edges or no-sharp leading edges on waveriders configuration becomes important. As was pointed in the introduction section, sharp leading edges are a dominant factor in the  $L/D$  ratio of waveriders as compared to conventional aerospace designs. Consequently, leading-edge bluntness introduced for manufacturing or heating concerns will result in a reduction on the  $L/D$  ratio. It should be emphasized in this context that, although the use of blunt leading edge can dramatically reduce the aerodynamic heating on the stagnation region of the vehicle, the aerodynamic performance is penalized since blunt leading edge allows leakage of the high-pressure flow from the lower surface region into the upper surface region, causing a reduction in the lift of the waverider.

## 5. CONCLUDING REMARKS

This study applies the Direct Simulation Monte Carlo method to assess the angle of attack effect on aerodynamic surface quantities of power-law shaped leading edges. The calculations provided information concerning the nature of the heat transfer, pressure, skin friction, drag and lift coefficients resulting from variations in the leading-edge shape at incidence for the idealized situation of two-dimensional hypersonic rarefied flow at 70 km of altitude. Performance results for 5, 10, 15 and 20 degrees of incidence for power-law exponents of 1/2, 2/3, 3/4 and 4/5 were compared to those cases for zero-degree angle of attack.

The analysis showed that the total drag coefficient increased as the leading-edge shape changed from sharp to blunt one at zero-degree angle of incidence. Nevertheless, at 20-degree angle of incidence, a significant decrease in the total drag coefficient was observed as compared as the leading-edge shape changed from sharp to blunt one. In addition, it was found that the lift coefficient decreased by increasing the power-law exponent of the leading edges. Moreover, the analysis verified that even the smaller leading edge bluntness resulted in significantly reduction on the lift-to-drag ratio. In this scenario, it can be inferred that a tradeoff between aerodynamic performance, lift-to-drag ratio, and aerodynamic heating, heat flux, is required for an optimal waverider design, since the heat flux is inversely proportional to the “nose radius” of the leading edge.

## 6. REFERENCES

- Bird, G. A., 1981, “Monte Carlo Simulation in an Engineering Context”, Progress in Astronautics and Aeronautics: Rarefied gas Dynamics, Ed. Sam S. Fisher, AIAA, New York, Vol. 74, part I, pp. 239–255.
- Bird, G. A., 1989, “Perception of numerical method in rarefied gasdynamics”, Progress in Astronautics and Aeronautics: Rarefied gas Dynamics, Eds. E. P. Muntz, and D. P. Weaver and D. H. Campbell, AIAA, New York, Vol. 118, pp. 374–395.
- Bird, G. A., 1994, “Molecular Gas Dynamics and the Direct Simulation of Gas Flows”, Oxford University Press, Oxford, England, UK.
- Borgnakke, C. and Larsen, P. S., 1975, “Statistical Collision Model for Monte Carlo Simulation of Polyatomic Gas Mixture”, Journal of computational Physics, Vol. 18, No. 4, pp. 405–420.
- Mason, W. H. and Lee, J., 1994, “Aerodynamically Blunt and Sharp Bodies”, Journal of Spacecraft and Rockets, Vol. 31, No. 3, pp. 378–382.
- Nonweiler, T. R. F., 1959, “Aerodynamic Problems of Manned Space Vehicles”, Journal of the Royal Aeronautical Society, Vol. 63, Sept., pp. 521–528.
- O’Brien, T. F. and Lewis, M. J., 1999, “Power Law Shapes for Leading-Edge Blunting with Minimal Shock Standoff”, Journal of Spacecraft and Rockets, Vol. 36, No. 5, pp. 653–658.
- Santos, W. F. N., and Lewis, M. J., 2002, “Power Law Shaped Leading Edges in Rarefied Hypersonic Flow”, Journal of Spacecraft and Rockets, Vol. 39, No. 6, pp. 917–925.
- Santos, W. F. N., and Lewis, M. J., 2005, “Aerothermodynamic Performance Analysis of Hypersonic Flow on Power-Law Leading Edges”, Journal of Spacecraft and Rockets, Vol. 42, No. 4, pp. 588–597.
- Santos, W. F. N., 2008, “Physical and Computational Aspects of Shock Waves over Power-Law Leading Edges”, Physics of Fluids, Vol. 20, No. 1, pp. 1070631-11.

## 7. Responsibility notice

The author is the only responsible for the printed material included in this paper.